Journal of Power Sources 446 (2020) 227338

Contents lists available at ScienceDirect

Journal of Power Sources

journal homepage: www.elsevier.com/locate/jpowsour

Li^+ conduction in air-stable Sb-Substituted Li_4SnS_4 for all-solid-state Li-Ion batteries

Hiram Kwak [a], Kern Ho Park [a], Daseul Han [b], Kyung-Wan Nam [b], Hyungsub Kim [c,**], Yoon Seok Jung [a,*]

[a] Department of Energy Engineering, Hanyang University, Seoul, 04763, South Korea
[b] Department of Energy and Materials Engineering, Dongguk University, Seoul, 04620, South Korea
[c] Korea Atomic Energy Research Institute, Daejeon, 34057, South Korea

HIGHLIGHTS

- Sb-substituted Li_4SnS_4 shows a maximum Li^+ conductivity of 0.85 mS cm^{-1} at 30 °C.
- Excellent dry-air stability and negligible H_2S evolution are confirmed.
- 1D-preferable 3D Li^+ diffusion channels disclosed by neutron diffraction analysis.
- Performance of all-solid-state Li-ion batteries using $Li_{3.85}Sn_{0.85}Sb_{0.15}S_4$.

GRAPHICAL ABSTRACT

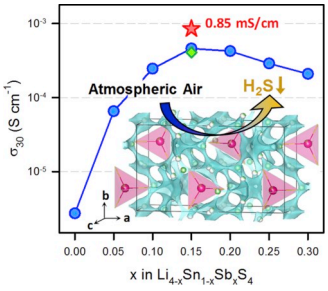

ARTICLE INFO

Keywords:
All-solid-state batteries
Solid electrolytes
Sulfides
Ionic conductivities
Neutron diffraction

ABSTRACT

Development of new sulfide Li^+ superionic conductors with mechanical sinterability is the key to the success of all-solid-state lithium batteries. While phosphorus-containing sulfide superionic conductor materials have been widely investigated, phosphorus-free materials showing good air-stability have been overlooked. Herein, the Li^+ dynamics in Sb-substituted Li_4SnS_4 showing a high Li^+ conductivity of max. 0.85 mS cm^{-1} at 30 °C and excellent dry-air stability as well as negligible H_2S evolution is described. Structural analysis with X-ray and neutron diffraction reveals that Sb-substitution renders an expansion of the lattice volume and formation of Li vacancies. Additionally, 1D-preferable 3D Li^+ diffusion channels in $Li_{4-x}Sn_{1-x}Sb_xS_4$ are disclosed. The fast Li^+ diffusion in $Li_{4-x}Sn_{1-x}Sb_xS_4$ is rationalized by complementary analysis using AC impedance measurements, bond valence energy landscape calculation, and ^7Li nuclear magnetic resonance spectroscopy. Excellent electrochemical performances of TiS_2 electrodes employing $Li_{3.85}Sn_{0.85}Sb_{0.15}S_4$ in all-solid-state batteries are demonstrated.

1. Introduction

Solidification of electrolytes using inorganic superionic conductors is vital for achieving safety and developing alternative electrode materials such as Li metal and S (or Li_2S) for next-generation rechargeable lithium batteries [1–6]. Among the various candidates for solid electrolytes

* Corresponding author.
** Corresponding author.
E-mail address: yoonsjung@hanyang.ac.kr (Y.S. Jung).

https://doi.org/10.1016/j.jpowsour.2019.227338
Received 5 July 2019; Received in revised form 18 September 2019; Accepted 18 October 2019
Available online 29 October 2019
0378-7753/

(SEs), sulfide materials show extremely high Li^+ conductivities of 10^{-3}-10^{-2} S cm^{-1} at room temperature [1,7–9]. Moreover, they are mechanically sinterable during the fabrication process for all-solid-state Li-ion or Li batteries (ASLBs), avoiding the hot sintering process that is accompanied by unwanted reactions between the SEs and active materials [1,10,11].

Despite these advantages, sulfide materials suffer from poor (electro) chemical stability [12–16]. Contrary to the belief that inorganic SEs have much wider electrochemical stability windows than conventional liquid electrolytes, recent theoretical and experimental studies have revealed that the intrinsic electrochemical stability windows of inorganic SEs are also narrow and passivating behaviors critically affect the performance of ASLBs, similar to the solid electrolyte interphase for conventional lithium-ion batteries [14,16–18]. Fortunately, engineering interfaces between SEs and active materials, such as the use of buffering phases, can facilitate reversible operation of ASLBs [13,19–21]. The evolution of toxic H_2S gases, when sulfide SE materials are exposed to ambient air, is also a challenging issue for the scale-up of ASLB technologies [1]. Moreover, sulfide SE materials degrade even under dry air conditions [12,15,22].

To date, the most popular sulfide SE materials that have been explored for ASLBs are based on Li_2S and P_2S_5. Several important glass-ceramic materials, such as β-Li_3PS_4 and $Li_7P_3S_{11}$, belong to the Li_2S–P_2S_5 system [1,8,23]. Argyrodite Li_6PS_5X (X = Cl, Br, I) was derived from the Li_2S–P_2S_5-LiX system [1,7]. Exploration of the Li_2S–P_2S_5-MS_2 (M = Ge, Si, Sn) system led to the identification of $Li_{10}GeP_2S_{12}$ families [1,9,24]. Notably, all these materials include phosphorus.

In contrast, despite their promising stabilities in atmospheric or dry air, only a few phosphorus-free SE materials have been explored so far, which might be due to their low Li^+ conductivities (<10^{-4} S cm^{-1}) [1, 25]. Liang and coworkers provided an important insight in their pioneering work on As-doped Li_4SnS_4, although the use of extremely toxic As avoids its practical application [26]. The low Li^+ conductivity of phosphorus-free Li_4SnS_4 (7.1×10^{-5} S cm^{-1}) could be dramatically enhanced to ~10^{-3} S cm^{-1} by the substitution of Sn with As and the resulting material showed good stability in air. The improvement in stability was explained by hard and soft acids and bases (HSAB) theory, which also agreed well with the results for phosphorus-free sulfide Na^+ superionic conductors such as Na_3SbS_4 and $Na_{4-x}Sn_{1-x}Sb_xS_4$ [22,27–29]. Phosphorus-free Li-ion SE materials developed to date include Li_4SnS_4 (~10^{-5} S cm^{-1} at room temperature) [15,25,26,30,31], Li_4SnSe_4 (2×10^{-5} S cm^{-1} at 20 °C) [32], Ge-doped Li_3AsS_4 (1.12×10^{-5} S cm^{-1} at 27 °C) [33], Li_2SnS_3 (1.6×10^{-3} S cm^{-1} at 100 °C) [34], $Li_{0.6}[Li_{0.2}Sn_{0.8}S_2]$ (9.3×10^{-3} S cm^{-1} at 25 °C (bulk conductivity)) [35], and 0.4LiI-0.6Li_4SnS_4 (4.1×10^{-4} S cm^{-1} at 30 °C) (Table S1) [15]. In our previous work, it was demonstrated that the incorporation of large and polarizable I^- ions in Li_4SnS_4 by the solution process using methanol increased the conductivity significantly [15]. However, the high conductivity was achieved for the glassy phase prepared by heat-treatment at low temperature (200 °C), reflecting a limitation of poor thermal stability.

Herein, we report the Li^+ conduction in phosphorus-free Li^+ superionic conductors, orthorhombic Sb-substituted Li_4SnS_4. Aliovalent substitution of Sn^{4+} in Li_4SnS_4 with Sb^{5+} drastically increases the Li^+ conductivity up to 8.5×10^{-4} S cm^{-1} at 30 °C (x = 0.15 in $Li_{4-x}Sn_{1-x}Sb_xS_4$), almost reaching ~10^{-3} S cm^{-1}. It is emphasized that the high conductivity of 8.5×10^{-4} S cm^{-1} with excellent dry-air-stability as well as negligible H_2S evolution upon exposure to atmospheric air is obtained together with a robust structural framework consisting of less toxic (especially in comparison with As), earth-abundant, environmentally benign elements. The fast Li^+ movements in the Sb-substituted Li_4SnS_4 are investigated by complementary analysis of neutron diffraction, ^{7}Li nuclear magnetic resonance (NMR) spectroscopy, and electrochemical impedance spectroscopy. Furthermore, TiS_2/Li–In all-solid-state cells employing $Li_{3.85}Sn_{0.85}Sb_{0.15}S_4$ demonstrate high capacity of 230 mA h g^{-1} at 30 °C with excellent cycling stability.

2. Results and discussion

The $Li_{4-x}Sn_{1-x}Sb_xS_4$ powders were prepared by solid-state synthesis using Li_2S, SnS_2, Sb_2S_3, and S powders as precursors at 550 °C. Fig. 1a shows the powder X-ray diffraction (XRD) patterns of $Li_{4-x}Sn_{1-x}Sb_xS_4$ over a wide range of x values ($0 \le x \le 0.30$). All the patterns match an orthorhombic Li_4SnS_4 with space group *Pnma* [25], implying the formation of a solid-solution phase. As the amount of Sb increases, shift in the peaks is observed. The single peak at ~25.8°, corresponding mainly to the (400) and (220) planes, is split and shifted slightly in a negative direction upon Sb-substitution, indicating asymmetric expansion of the lattice volume in the *a* direction. It is noted that impurity peaks such as that at ~17.0° (denoted by the downward arrow, not identical to the impurity observed at x = 0.00) start to appear at x = 0.15, from which the solubility limit is determined as $0.10 < x < 0.15$.

Fig. 1b shows that the crystal structure of $Li_{4-x}Sn_{1-x}Sb_xS_4$ comprises isolated Sn/SbS_4 tetrahedra and four distinct Li sites. The ionic radius of Sb^{5+} (74 pm for coordination number (CN) = 6) is smaller than that of Sn^{4+} (83 pm for CN = 6, 69 pm for CN = 4, comparison of the ionic radii for CN = 6 is because the ionic radius of Sb^{5+} for CN = 4 is not available) [36]. Thus, the volume of the SbS_4 tetrahedra is also smaller than that of the SnS_4 tetrahedra, as evidenced by the extended X-ray absorption fine structure (EXAFS) fitting results showing the shorter Sb–S bond length (2.33(8) Å) than that of Sn–S (2.39(3) Å, Figure S1, Table S2). In this regard, the shrinkage of the lattice volume upon Sb-substitution may be expected, which turns out not to be the case. Excellent fitting results of both Sn and Sb K-edge EXAFS spectra using the same model structure of orthorhombic Li_4SnS_4 (*Pnma* space group) also confirm the successful substitution of the Sn site by Sb (i.e., formation of the solid-solution phase). The changes in the lattice constants and the corresponding lattice volume as a function of the amount of substituted Sb are shown in Fig. 1c and S2. In the range of $0 \le x \le 0.10$, a sharp asymmetric increase of the lattice volume in the *a* direction is observed. In this range, the lattice slightly shrinks and expands in the *b* and *c* directions, respectively. The higher electronegativity of Sb^{5+} (1.971) than that of Sn^{4+} (1.706) indicates lesser electron density of S in Sb–S as compared to that in Sn–S [37–39]. Consequently, the bond strength of Li–S for Sb-substituted Li_4SnS_4 is likely lowered throughout the lattice, which could explain the increased average Li–S bond length, as reflected by the increased average volume of LiS_x polyhedra (Table S3). This may be in line with the overall expanded lattice volume of Sb-substituted Li_4SnS_4. At $x \ge 0.10$, the lattice constants remain relatively constant, which is in good agreement with the solubility limit of Sb in Li_4SnS_4 ($0.10 < x < 0.15$), as estimated by the presence of the impurity phase (Fig. 1a).

When exposed to water, Li_4SnS_4 forms hydrate phases without suffering from evolution of toxic H_2S [25,30]. The Sb-substituted Li_4SnS_4 ($Li_{3.85}Sn_{0.85}Sb_{0.15}S_4$) also showed the excellent air stability (Fig. 2). Upon exposure to atmospheric air (~50% of relative humidity) at room temperature, in contrast to the large amount of H_2S evolved for conventional phosphorus-containing Li_6PS_5Cl (max. 89 ppm), H_2S evolution for $Li_{3.85}Sn_{0.85}Sb_{0.15}S_4$ was negligible (max. 6 ppm, trace amounts of impurities such as Li_2S may be responsible for the extremely low but existing H_2S).

The smooth surface of cold-pressed Sb-doped Li_4SnS_4 powders indicates excellent mechanical sinterability (Figure S3). The variation of Li^+ conductivities at 30 °C as a function of Sb substitution (x) in a series of $Li_{4-x}Sn_{1-x}Sb_xS_4$ is displayed in Fig. 3. The Li^+ conductivities were obtained by fitting the Nyquist plot for Li^+-ion-blocking Ti/$Li_{4-x}Sn_{1-x}Sb_xS_4$/Ti symmetric cells, where cold-pressed SE pellets were prepared, using the equivalent circuit model (Figure S4). The Nyquist plots show the depressed semicircle followed by the capacitive Warburg-like tail, which is a typical shape for solid ionic conductors showing a negligible contribution of electrons as a charge carrier [18,40]. Without Sb substitution (x = 0.00), the Li^+ ion conductivity is 2.7×10^{-6} S cm^{-1}. This value is lower than that obtained in the previous report [25], which

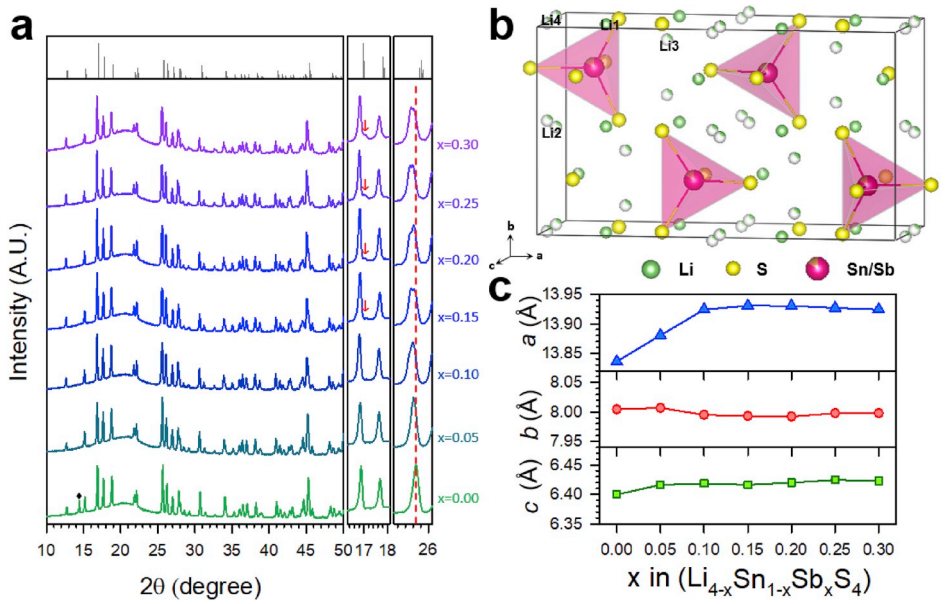

Fig. 1. Structural characterization of Sb-doped Li_4SnS_4 ($Li_{4-x}Sn_{1-x}Sb_xS_4$ ($0 \leq x \leq 0.30$)). a) Powder X-ray diffraction patterns. The Bragg peaks for Li_4SnS_4 are shown at the top.[25] b) Crystal structure of Sb-doped Li_4SnS_4 with unit cell outlined. c) Lattice parameters as a function of the amount of Sb doped (x).

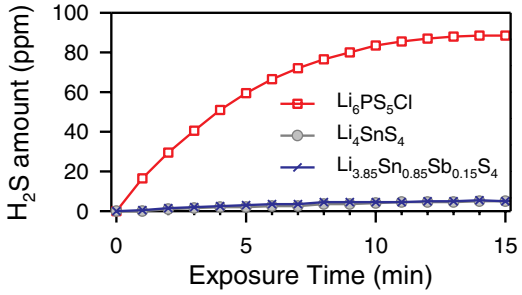

Fig. 2. H_2S amount as a function of time in atmospheric air for $Li_{3.85}Sn_{0.85}Sb_{0.15}S_4$, compared with Li_6PS_5Cl or Li_4SnS_4.

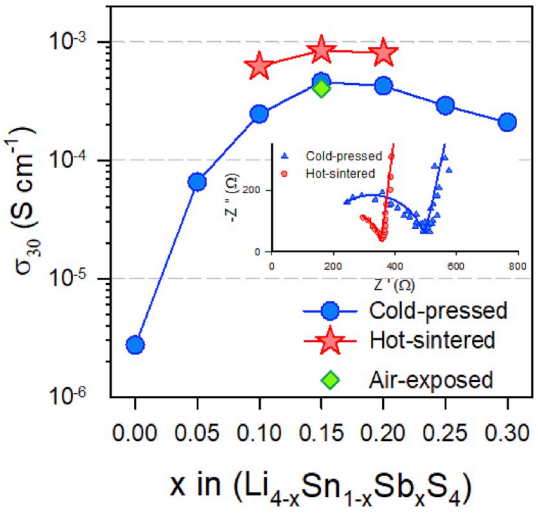

Fig. 3. Li^+ conductivities at 30 °C for $Li_{4-x}Sn_{1-x}Sb_xS_4$. Typical Nyquist plots are also shown in the inset.

could be attributed to trace amounts of impurities, as shown in Fig. 1a (denoted by '◆'). As the amount of substituted Sb increases, Li^+ conductivity drastically increases up to $x = 0.15$ by more than two orders of magnitude and shows a maximum value of 4.6×10^{-4} S cm^{-1}. The activation energy E_a is lowered from 0.56 ($x = 0.00$) to 0.50 eV ($x = 0.15$, Figure S5, the Arrhenius plots are shown in Figure S6). Moreover, the hot-sintered pellet for $Li_{3.85}Sn_{0.85}Sb_{0.15}S_4$ achieved a Li^+ conductivity of 8.5×10^{-4} S cm^{-1} ($E_a = 0.43$ eV). This value is comparable with the record for phosphorus-free Li-ion SEs (As-substituted Li_4SnS_4, Table S1) [26]. Furthermore, $Li_{3.85}Sn_{0.85}Sb_{0.15}S_4$ shows marginal degradation in Li^+ conductivity and structure after exposure to dry air with a relative humidity of ~0% for 12 h at room temperature (4.1×10^{-4} S cm^{-1}, Fig. 3, S7), which could be rationalized by the HSAB theory; soft acids Sn^{4+} and Sb^{5+} are less reactive to hard base O^{2-} than hard acid P^{5+} [15,22 26].

The overall variation of Li^+ conductivity shown in Fig. 3, i.e., the drastic increase up to $x = 0.15$ and the subsequent slight decrease, could reveal an underlying mechanism responsible for the significantly enhanced Li^+ conductivity by Sb-substitution in Li_4SnS_4. First, the aliovalent substitution of Sn^{4+} with Sb^{5+} leads to the formation of Li vacancies, which could contribute to the increased Li^+ conductivity. While the unsubstituted Li_4SnS_4 has fully occupied Li sites (Li1 and Li2: occupancies of ~1.00), the Sb-substitution for Li_4SnS_4 renders to create Li vacancies in Li2-4 sites, which will be discussed in detail later. Second, the trend of Li^+ conductivities as a function of Sb-substitution follows that of the overall lattice volume (Fig. 1a and c, S2), indicating their strong correlation. The slight decrease of Li^+ conductivity as x increases from 0.15 to 0.30, which appears to be marginally deviating from the relatively constant lattice volume (Figure S2a), is attributed to the increased amount of the impurity phase. During preparation of this manuscript, we became aware of similar work [41]. Their work showed the decreasing lattice size upon the substitution of Sn^{4+} with Sb^{5+}, which is contrasted by our result. Interestingly, the aliovalent substitution of Sn^{4+} in Li_4SnS_4 with Sb^{3+} resulted in the enlarged lattice volume and the enhanced Li^+ conductivity (2.75×10^{-5} S cm^{-1} for $Li_{4.05}Sn_{0.95}Sb_{0.05}S_4$ at 30 °C, Figure S2b). The expanded lattice volume is considered to offer an increased volume of Li^+ transport paths [42–46]. The increased average Li–S bond length upon Sb-substitution is believed to render favorable energy landscape for facile Li^+ migration (Table S3) [47]. However, this rationale may be contradicted by the low ionic

conductivity of Li_4SnSe_4 which was comparable to that of Li_4SnS_4 in the previous report [32]. Zeier and coworkers provided an insight that introducing large and polarizable ions affected the ionic migration by lowering not only the activation barriers but also the pre-factors, which blurred determination of whether the overall ionic conductivity would be enhanced or not [48]. Following this theory, our result implies that the enlarged lattice volume (thereby, the lowered activation barriers) with preserved sulfide anion and increased Li^+ vacancies might be the key to the overall enhancement of Li^+ conductivity.

In order to gain more insight on the fast Li^+ transport in Sb-substituted Li_4SnS_4 from the structural point of view, powder neutron diffraction was carried out for $Li_{4-x}Sn_{1-x}Sb_xS_4$ (x = 0.00, 0.10, 0.15, 0.20). The powder neutron Rietveld refinement profile for $Li_{3.85}Sn_{0.85}Sb_{0.15}S_4$ is shown in Fig. 4a, and the refinement results are summarized in Table 1. The refinement procedures and results for other compositions (x = 0.00, 0.10, 0.20) are shown in the Experimental Section and Supporting Information (Figure S8, and Tables S4-6). While Li1 and Li2 sites are tetrahedrally coordinated, Li3 and Li4 sites are located in distorted octahedra. The Li occupancies are shown in Fig. 5 and Tables S4-6. The tetrahedral Li1 site is fully occupied in the whole range of x in $Li_{4-x}Sn_{1-x}Sb_xS_4$. The occupancy of tetrahedral Li2 site at x = 0.00 is also close to unity. In contrast, the occupancies of the octahedral sites, Li3 and Li4, at x = 0.00 are ~1/4. By the aliovalent substitution of Sn^{4+} with Sb^{5+}, occupancies for Li2, Li3, and Li4 are decreased. The creation of Li vacancy in Li2 site (that is fully occupied in the undoped Li_4SnS_4) may be the key to the drastic enhancement of Li^+ conductivity upon Sb-substitution. The decrease in Li occupancies is more severe for the octahedral sites than for the tetrahedral sites, which is consistent with the ^6Li magic angle spinning (MAS) NMR spectral results (Figure S9).

The bond valence energy landscape (BVEL) map for $Li_{3.85}Sn_{0.85}Sb_{0.15}S_4$ was obtained using the results of neutron diffraction

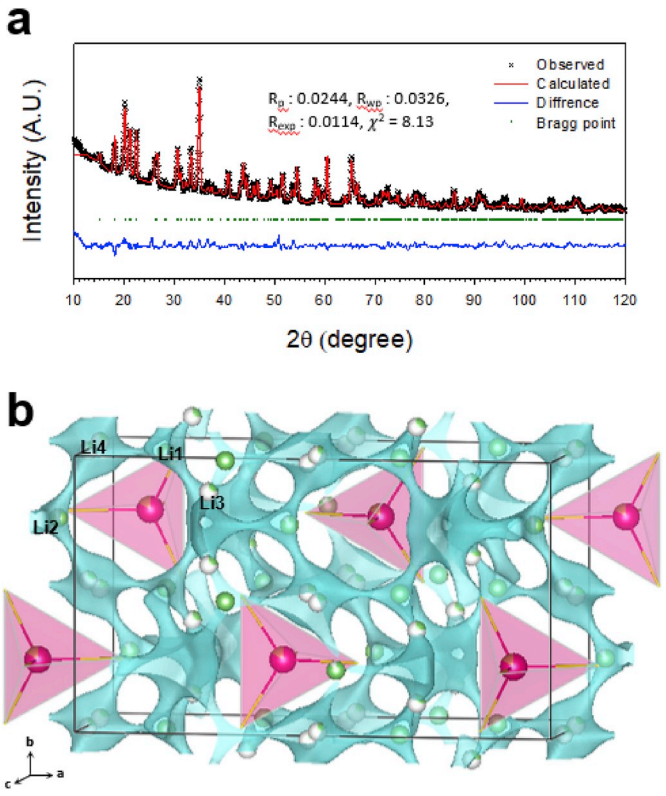

Fig. 4. Results of neutron diffraction for $Li_{4-x}Sn_{1-x}Sb_xS_4$ (x = 0.15). a) Observed and calculated neutron Rietveld refinement profile for $Li_{3.85}Sn_{0.85}Sb_{0.15}S_4$. b) 3D Li^+ diffusion paths for $Li_{3.85}Sn_{0.85}Sb_{0.15}S_4$ obtained by the BVEL calculations with an iso-surface value of ±0.7 v.u.

Table 1
Crystallographic data and neutron diffraction Rietveld refinement results for $Li_{4-x}Sn_{1-x}Sb_xS_4$ with x = 0.15.

Crystal System	Orthorhombic
Space Group	P n m a (No. 62)
Lattice Parameter, Volume	a = 13.9256(15) Å, b = 7.9897(9) Å, c = 6.4154(7) Å, V = 713.78(14) Å^3

Atom	x	y	z	Wyckoff	Occupancy	B_{iso}
Li1	0.3324 (11)	0.4953 (15)	0.194(2)	8d	1	4.8(2)
Li2	0.5619 (13)	0.25	0.158(3)	4c	0.89(1)	4.8(2)
Li3	0.212(4)	0.383(5)	0.576(8)	8d	0.24(2)	4.8(2)
Li4	0.488(7)	0.516 (13)	−0.01(2)	8d	0.22(1)	4.8(2)
Sn1	0.4098 (4)	0.25	0.6561 (7)	4c	0.85	2.00 (12)
Sb1	0.4098 (4)	0.25	0.6561 (7)	4c	0.15	2.00 (12)
S1	0.4097 (7)	0.25	0.2801 (11)	4c	1	0.61 (20)
S2	0.5775 (9)	0.25	0.7759 (13)	4c	1	1.9(2)
S3	0.3305 (6)	0.4931 (9)	0.7747 (13)	8d	1	2.66 (17)

R_p: 2.44, R_{wp}: 3.26, R_{exp}: 1.14, χ^2 = 8.13.

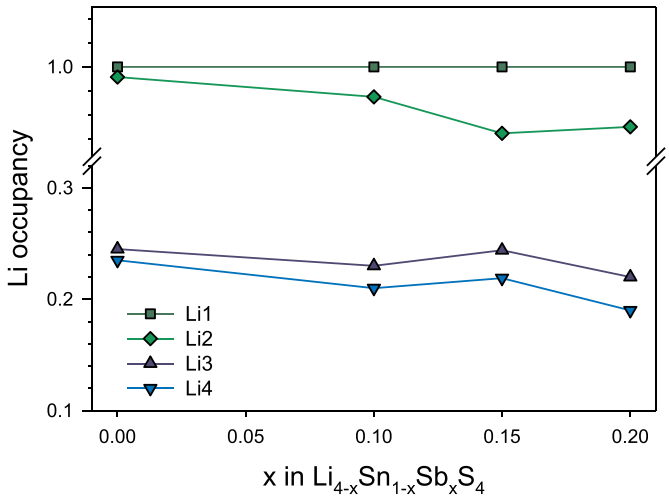

Fig. 5. Li occupancies as a function of x in $Li_{4-x}Sn_{1-x}Sb_xS_4$.

(Fig. 4b), which indicates possible Li^+ diffusion pathways [28,49]. From this result, in addition to the four Li sites, we suggest that a Li^+ interstitial site (Li_{int}) is located at the fractional coordinates (0.75, 0.75, 0.9753) in the distorted S-surrounding octahedra. The resulting Li^+ migration pathways are shown using the ball-and-stick illustration (Fig. 6) and the interconnected Li–S_n polyhedra illustration (Figure S10). Li^+ could migrate from the highly occupied tetrahedral sites to octahedral sites with low occupancies of <1/4 or octahedral interstitial sites, and vice versa. Investigation of the as-developed Li^+ migration pathways allowed us to identify four unique Li^+ paths (Fig. 6, Table S7); Li2–Li4–Li2–Li4 (path 1), Li3–Li1–Li_{int}–Li1–Li3 (path 2), Li4–Li2–Li3–Li_{int}–Li1–Li4 (path 3), and Li4–Li1–Li_{int}–Li1–Li4 (path 4). Furthermore, the Li^+ migration energy landscape diagram for Li_4SnS_4 and $Li_{3.85}Sn_{0.85}Sb_{0.15}S_4$ was obtained by the BVEL calculation (Figure S11), allowing for acquiring the activation energies for each of the Li^+ migration pathways (Table S7) [50,51]. The activation energy is lowered by the Sb-substitution (e.g., path 2: from 0.563 to 0.539 eV). This result agrees well with those obtained by the AC impedance method (Figure S5), and could contribute to the drastic increase in the Li^+ conductivity of Sb-substituted Li_4SnS_4. Path 3, representing migration in

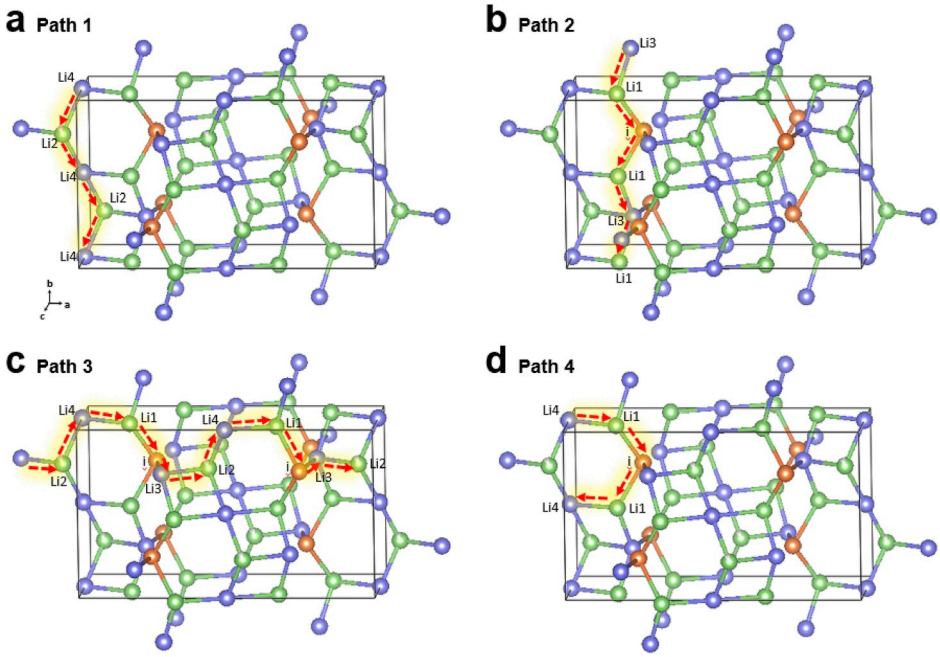

Fig. 6. Possible Li^+ conduction paths derived from the BVEL calculations (Fig. 4b). The interstitial site is denoted as 'i'.

distorted *a* and *c* directions, shows the highest activation energy (0.640 eV for $Li_{3.85}Sn_{0.85}Sb_{0.15}S_4$). Considering that paths 1 and 2 are all in the *b* direction and path 4 could be combined with path 1, Sb-substituted Li_4SnS_4 likely preferred 1D Li^+ conduction pathways. The anisotropic expansion of the lattice volume in the *a* direction upon Sb-substitution indicates the increased size of Li^+ diffusion channels in the *b* direction (paths 1 and 2), which could render more facile Li^+ movements.

Temperature-dependent static ^7Li NMR spectra and spin-lattice relaxation ($1/T_1$) for Li_4SnS_4 and $Li_{3.85}Sn_{0.85}Sb_{0.15}S_4$ were obtained to acquire information about local Li^+ dynamics. Fig. 7a shows the static ^7Li NMR spectra recorded at varied temperatures. At the low temperature of 180 K, both spectra show broad peaks, indicating ^7Li dipole-dipole interactions [52,53]. As Li^+ movements accelerate with increasing temperature, ^7Li dipole-dipole interactions are averaged out and the broad spectra become narrower, which is termed as motional narrowing [52,53]. At 240 K, the motional narrowing becomes significant for $Li_{3.85}Sn_{0.85}Sb_{0.15}S_4$, whereas the spectrum for Li_4SnS_4 remains broadened. A much lower onset temperature for the motional narrowing for $Li_{3.85}Sn_{0.85}Sb_{0.15}S_4$ than for Li_4SnS_4 is clearly seen in Fig. 7b. The static ^7Li NMR spin-lattice relaxation rate ($1/T_1$) result is shown in Fig. 7c. The temperature at which the relaxation rate ($1/T_1$) is maximum indicates the equivalent Li^+ hopping and Larmor frequencies [52,53]. The maximum $1/T_1$ for $Li_{3.85}Sn_{0.85}Sb_{0.15}S_4$ is observed at 405 K, which is lower than that for Li_4SnS_4 (420 K). Both the motional narrowing behaviors and the spin-lattice relaxation rates indicate faster Li^+ movements in $Li_{3.85}Sn_{0.85}Sb_{0.15}S_4$ for Li_4SnS_4. Moreover, the activation energy obtained in the low temperature range is much lower for $Li_{3.85}Sn_{0.85}Sb_{0.15}S_4$ (0.16 eV) than for Li_4SnS_4 (0.30 eV).

In short, the drastic enhancement of Li^+ conductivity with the lowered activation energy for the Sb-substituted Li_4SnS_4 is supported unequivocally by the results of neutron diffraction and ^7Li NMR. Although the effects of asymmetrically enlarged lattice volume and the lowered Li occupancies (or increased Li vacancies) by Sb-substitution on Li^+ conductivity have been discussed, the origin still remains unclear and has been the subject of theoretical calculations [44,47,54–56].

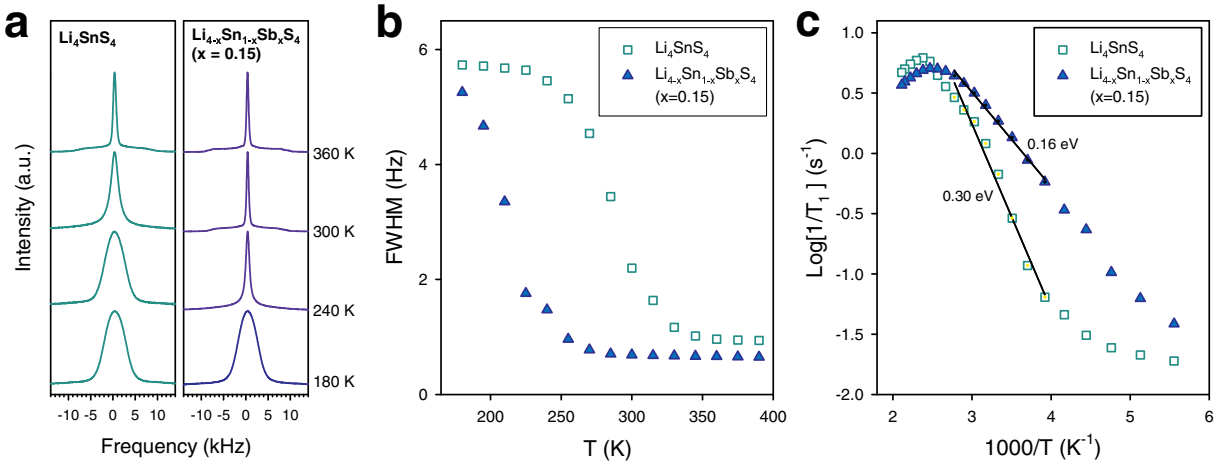

Fig. 7. Results of ^7Li static NMR for Li_4SnS_4 and $Li_{3.85}Sn_{0.85}Sb_{0.15}S_4$. a) ^7Li NMR spectra. b) Motional narrowing of the ^7Li NMR linewidth c) ^7Li NMR spin−lattice relaxation rate $1/T_1$ at different temperatures. The activation energy values obtained in the low-temperature range are also shown.

Finally, TiS_2/Li–In all-solid-state cells fabricated using $Li_{3.85}Sn_{0.85}Sb_{0.15}S_4$ were cycled between 1.5 and 3.0 V (vs. Li/Li^+) at 30 °C. Fig. 8a shows the first two-cycle discharge-charge voltage profiles for the cell using $Li_{3.85}Sn_{0.85}Sb_{0.15}S_4$ at 0.05 C. The TiS_2 electrode employing $Li_{3.85}Sn_{0.85}Sb_{0.15}S_4$ exhibits reversible capacities of 230 mA h g^{-1}, which almost reaches the theoretical capacity of TiS_2 (239 mA h g^{-1}). Moreover, TiS_2/Li–In all-solid-state cells using $Li_{3.85}Sn_{0.85}Sb_{0.15}S_4$ shows a remarkable rate capability. A capacity retention of 57% with respect to the capacity at 0.05C is achieved (Fig. 8b). Furthermore, TiS_2/Li–In cells using $Li_{3.85}Sn_{0.85}Sb_{0.15}S_4$ shows excellent cycling stability (capacity retention of 99.2% after 80 cycles with respect to the capacity at third cycle).

3. Conclusions

In summary, a Li^+ superionic conductor, $Li_{4-x}Sn_{1-x}Sb_xS_4$ ($0 < x < 0.15$), showing a maximum Li^+ conductivity of 0.85 mS cm^{-1} at 30 °C and negligible H_2S evolution upon exposure to atmospheric air, was investigated. The significant enhancement in Li^+ conduction with the lowered activation energy upon Sb-substitution was confirmed by AC impedance and ^{7}Li NMR spectroscopy measurements. Structural analysis showed that the aliovalent Sb substitution resulted in the anisotropic expansion of lattice volume in the *a* direction and the formation of Li vacancies, which could explain the drastic increase in Li^+ conductivity. Moreover, BVEL analysis revealed that the 3D Li^+ diffusion channels had a preference for 1D diffusion along the *b* direction and activation barriers were lowered by Sb-substitution. Finally, the excellent electrochemical performance of TiS_2/Li–In all-solid-state cells using $Li_{3.85}Sn_{0.85}Sb_{0.15}S_4$ was highlighted. The results of this study provide an important insight into the design of new superionic conductors and development of practical all-solid-state technologies.

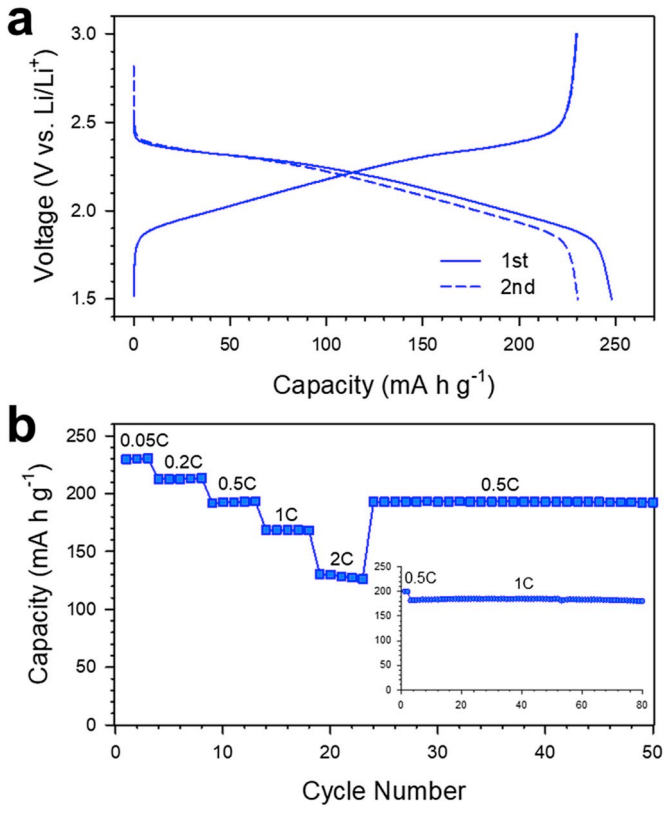

Fig. 8. Electrochemical performances of the TiS_2 electrodes employing $Li_{3.85}Sn_{0.85}Sb_{0.15}S_4$ in TiS_2/Li–In all-solid-state cells at 30 °C. a) First two-cycle discharge-charge voltage profiles at 0.05C for TiS_2 electrode using $Li_{3.85}Sn_{0.85}Sb_{0.15}S_4$. b) Charge capacities of TiS_2 electrodes using $Li_{3.85}Sn_{0.85}Sb_{0.15}S_4$ as a function of the cycle number at different C-rates. Cycling performance is also shown in the inset.

4. Experimental

4.1. Preparation of materials

For the synthesis of $Li_{4-x}Sn_{1-x}Sb_xS_4$ powders, a stoichiometric mixture of Li_2S (99.9%, Alfa Aesar), SnS_2 (99%, MKN), Sb_2S_3 (99.5%, Sigma Aldrich), and S (99.5%, Alfa Aesar) was heat-treated at 550 °C for 12 h in a fused silica ampoule sealed under vacuum. Li_3PS_4 powders were prepared by mechano-chemical milling of a stoichiometric mixture of Li_2S and P_2S_5 (99%, Sigma Aldrich), followed by heat-treatment at 243 °C for 1 h in a glass ampoule sealed under vacuum. Li_6PS_5Cl powders were prepared by mechano-chemical milling and subsequent heat treatment [21]. A stoichiometric mixture of Li_2S (99.9%, Alfa Aesar), P_2S_5 (99%, Sigma Aldrich), and LiCl (99.99%, Sigma-Aldrich) was ball-milled at 600 rpm in a ZrO_2 vial with ZrO_2 balls using Pulverisette 7 PL (Fritsch GmbH). The resulting powders were heat-treated at 550 °C under Ar atmosphere.

4.2. Materials characterization

The powder XRD patterns were collected using a Rigaku MiniFlex 600 diffractometer with Cu K_α radiation ($\lambda = 1.5406$ Å). XRD cells containing hermetically sealed SE samples with a beryllium window were mounted on a XRD diffractometer and measured at 40 kV and 15 mA. The neutron powder diffraction data were obtained from the HANARO facility in the Korea Atomic Energy Research Institute (KAERI). The measurements were conducted at a 2θ range of 0–160° with a step size of 0.05° using a wavelength of 1.834707 Å. X-ray and neutron diffraction data were refined by the Rietveld refinement method using Fullprof software. Pseudo-Voigt function was used for approximation of the experimental neutron diffraction patterns, and variables for profile function such as U, V, W, shape, asymmetric parameters were obtained from standard reference material of Si640e. The refinement was started with atomic coordinates reported by Kaib et al. [25]. All fractional atomic coordinates are allowed to relax freely with symmetric restriction, and equivalent isotropic thermal parameter (B_{iso}) was applied for all Li sites due to the disorder which may be caused from partially occupied Li. Atomic ratios of Sn to Sb obtained from inductively coupled plasma optical emission spectroscopy (ICP-OES) results were used for the Rietveld refinement, and the Li occupancies in each site were allowed to relax freely during Rietveld refinement. The empirical bond valence-based softBV method developed by S. Adams was employed [57]. The BVEL calculations were carried out by transforming the valence units into energy units by using BondStr program implemented in the Fullprof Suite. Sn and Sb K-edge X-ray absorption spectroscopic measurements were performed at the 10C beamline of the Pohang Accelerator Laboratory (PAL) using a Si (111) double-crystal monochromator in transmission mode. Reference spectra of Sn and Sb metallic foils were collected simultaneously for energy calibration. X-ray absorption near edge structure (XANES) and EXAFS data were handled and processed using the Athena and Artemis programs. The extracted EXAFS signal, $\chi(k)$, was weighted by k^2 to emphasize the high-energy oscillations, and then Fourier-transformed in *k*-ranges of 3.0–13.5 $Å^{-1}$ for Sn and Sb, using a Hanning window function to obtain the magnitude plots of the EXAFS spectra in R-space (Å). Temperature-dependent static ^{7}Li NMR spectra and spin-lattice relaxation rate ($1/T_1$) measurements were obtained using a 400 MHz Advance II+ system (Bruker solid-state NMR) at the KBSI Seoul Western Center, for which the ^{7}Li resonance frequency was 155.506 MHz. NMR sample powders were sealed in a 4 mm ZrO_2 rotor in an Ar-filled glove box; all signals were obtained after a π/2 pulse in the temperature range of 180–435 K. An external chemical shift reference of LiCl powder spun at 4 kHz was calibrated to 0 ppm. ^{6}Li MAS NMR spectra were obtained on a 400 MHz Advance II + system

(Bruker solid-state NMR) at 58.862 MHz and a rotation frequency of 10 kHz. The amount of H_2S was measured using an H_2S sensor (SP2297, SENKO). The SE powder samples were kept in a closed 2.6 L chamber filled with atmospheric air with a relative humidity of ~50% at room temperature. The air inside the chamber was circulated using a small electric fan.

4.3. Electrochemical characterization

The Li^+ conductivity was measured by the AC impedance method using ion-blocking Ti/$Li_{4-x}Sn_{1-x}Sb_xS_4$/Ti symmetric cells. The cold-pressed pellets were prepared at 370 MPa and the hot-sintered pellets were prepared by heat-treatment of the cold-pressed pellets at 550 °C. All-solid-state TiS_2/Li–In half-cells were fabricated by the following procedure: The Li–In (nominal composition: $Li_{0.5}In$) as the counter and reference electrodes were prepared by ball-milling In (Aldrich, 99%) and Li (FMC Lithium Corp.) powders according to our previous report.[10] Composite electrodes were prepared from a TiS_2/$Li_{3.85}Sn_{0.85}Sb_{0.15}S_4$ mixture in a weight ratio of 1:2. The separating SE layers were formed by pelletizing 150 mg of Li_3PS_4 powders under 370 MPa. Then, the TiS_2 electrodes and the Li–In electrodes were put on each side of the SE layers. Finally, the whole assemblies were pressed at 370 MPa, forming all-solid-state TiS_2/Li–In cells. Galvanostatic discharge-charge cycling of the all-solid-state TiS_2/Li–In cells was carried out in the voltage range of 1.5–3.0 V (vs. Li/Li^+). All the procedures to fabricate all-solid-state cells were performed in a polyaryletheretherketone (PEEK) mold (diameter = 13 mm) with Ti rods as current collectors. All electrochemical tests were conducted at 30 °C.

Acknowledgements

This research was supported by the Technology Development Program to Solve Climate Changes and by Basic Science Research Program of the National Research Foundation (NRF) funded by the Ministry of Science & ICT (grant no. NRF-2017M1A2A2044501, 2018R1A2B6004996, and 2017M1A2A2044502), and by the Materials and Components Technology Development Program of MOTIE/KEIT (grant no. 10077709).

Appendix A. Supplementary data

Supplementary data related to this article can be found at https://doi.org/10.1016/j.jpowsour.2019.227338.

References

[1] K.H. Park, Q. Bai, D.H. Kim, D.Y. Oh, Y. Zhu, Y. Mo, Y.S. Jung, Adv. Energy Mater. 8 (2018) 1800035.
[2] A. Manthiram, X. Yu, S. Wang, Nat. Rev. Mater. 2 (2017) 16103.
[3] J. Schnell, T. Günther, T. Knoche, C. Vieider, L. Köhler, A. Just, M. Keller, S. Passerini, G. Reinharta, J. Power Sources 382 (2018) 160–175.
[4] R. Schmuch, R. Wagner, G. Hörpel, T. Placke, M. Winter, Nat. Energy 3 (2018) 267–278.
[5] X. Han, Y. Gong, K.K. Fu, X. He, G.T. Hitz, J. Dai, A. Pearse, B. Liu, H. Wang, G. Rubloff, Y. Mo, V. Thangadurai, E.D. Wachsman, L. Hu, Nat. Mater. 16 (2017) 572–579.
[6] Y. Yan, R.-S. Kühnel, A. Remhof, L. Duchêne, E.C. Reyes, D. Rentsch, Z. Łodziana, C. Battaglia, Adv. Energy Mater. 7 (2017) 1700294.
[7] H.-J. Deiseroth, S.-T. Kong, H. Eckert, J. Vannahme, C. Reiner, T. Zaiss, M. Schlosser, Angew. Chem. Int. Ed. 47 (2008) 755–758.
[8] Y. Seino, T. Ota, K. Takada, A. Hayashi, M. Tatsumisago, Energy Environ. Sci. 7 (2014) 627–631.
[9] Y. Kato, S. Hori, T. Saito, K. Suzuki, M. Hirayama, A. Mitsui, M. Yonemura, H. Iba, R. Kanno, Nat. Energy 1 (2016) 16030.
[10] Y.J. Nam, K.H. Park, D.Y. Oh, W.H. An, Y.S. Jung, J. Mater. Chem. A 6 (2018) 14867–14875.
[11] D.Y. Oh, Y.J. Nam, K.H. Park, S.H. Jung, K.T. Kim, A.R. Ha, Y.S. Jung, Adv. Energy Mater. 9 (2019) 1802927.
[12] H. Muramatsu, A. Hayashi, T. Ohtomo, S. Hama, M. Tatsumisago, Solid State Ion. 182 (2011) 116–119.
[13] A. Sakuda, A. Hayashi, M. Tatsumisago, Chem. Mater. 22 (2010) 949–956.
[14] Y. Zhu, X. He, Y. Mo, ACS Appl. Mater. Interfaces 7 (2015) 23685–23693.
[15] K. Park, B.C. Yu, J.W. Jung, Y.T. Li, W.D. Zhou, H.C. Gao, S. Son, J.B. Goodenough, Chem. Mater. 28 (2016) 8051–8059.
[16] S. Wenzel, T. Leichtweiss, D.A. Weber, J. Sann, W.G. Zeier, J. Janek, ACS Appl. Mater. Interfaces 8 (2016) 28216–28224.
[17] K. Xu, Chem. Rev. 114 (2014) 11503–11618.
[18] B.R. Shin, Y.J. Nam, D.Y. Oh, D.H. Kim, J.W. Kim, Y.S. Jung, Electrochim. Acta 146 (2014) 395–402.
[19] N. Ohta, K. Takada, L. Zhang, R. Ma, M. Osada, T. Sasaki, Adv. Mater. 18 (2006) 2226–2229.
[20] J.H. Woo, J.J. Travis, S.M. George, S.-H. Lee, J. Electrochem. Soc. 162 (2015) A344–A349.
[21] S.H. Jung, K. Oh, Y.J. Nam, D.Y. Oh, P. Bruener, K. Kang, Y.S. Jung, Chem. Mater. 30 (2018) 8190–8200.
[22] A. Banerjee, K.H. Park, J.W. Heo, Y.J. Nam, C.K. Moon, S.M. Oh, S.-T. Hong, Y. S. Jung, Angew. Chem. Int. Ed. 55 (2016) 9634–9638.
[23] K. Homma, M. Yonemura, T. Kobayashi, M. Nagao, M. Hirayama, R. Kanno, Solid State Ion. 182 (2011) 53–58.
[24] N. Kamaya, K. Homma, Y. Yamakawa, M. Hirayama, R. Kanno, M. Yonemura, T. Kamiyama, Y. Kato, S. Hama, K. Kawamoto, A. Mitsui, Nat. Mater. 10 (2011) 682–686.
[25] T. Kaib, S. Haddadpour, M. Kapitein, P. Bron, C. Schroeder, H. Eckert, B. Roling, S. Dehnen, Chem. Mater. 24 (2012) 2211–2219.
[26] G. Sahu, Z. Lin, J. Li, Z. Liu, N. Dudney, C. Liang, Energy Environ. Sci. 7 (2014) 1053–1058.
[27] T.W. Kim, K.H. Park, Y.E. Choi, J.Y. Lee, Y.S. Jung, J. Mater. Chem. A 6 (2018) 840–844.
[28] J.W. Heo, A. Banerjee, K.H. Park, Y.S. Jung, S.-T. Hong, Adv. Energy Mater. 8 (2018) 1702716.
[29] L. Zhang, D. Zhang, K. Yang, X. Yan, L. Wang, J. Mi, B. Xu, Y. Li, Adv. Sci. 3 (2016) 1600089.
[30] Y.E. Choi, K.H. Park, D.H. Kim, D.Y. Oh, H.R. Kwak, Y.-G. Lee, Y.S. Jung, ChemSusChem 10 (2017) 2605–2611.
[31] K. Kanazawa, S. Yubuchi, C. Hotehama, M. Otoyama, S. Shimono, H. Ishibashi, Y. Kubota, A. Sakuda, A. Hayashi, M. Tatsumisago, Inorg. Chem. 57 (2018) 9925–9930.
[32] T. Kaib, P. Bron, S. Haddadpour, L. Mayrhofer, L. Pastewka, T.T. Jaervi, M. Moseler, B. Roling, S. Dehnen, Chem. Mater. 25 (2013) 2961–2969.
[33] G. Sahu, E. Rangasamy, J. Li, Y. Chen, K. An, N. Dudney, C. Liang, J. Mater. Chem. A 2 (2014) 10396–10403.
[34] J.A. Brant, D.M. Massi, N.A.W. Holzwarth, J.H. MacNeil, A.P. Douvalis, T. Bakas, S. W. Martin, M.D. Gross, J.A. Aitken, Chem. Mater. 27 (2015) 189–196.
[35] T. Holzmann, L.M. Schoop, M.N. Ali, Moudrakovski, G. Gregori, J. Maier, R. J. Cavad, B.V. Lotsch, Energy Environ. Sci. 9 (2016) 2578–2585.
[36] J.E. Huheey, E.A. Keiter, R.L. Keiter, O.K. Medhi, Inorganic Chemistry: Principles of Structure and Reactivity, Pearson Education India, 2006.
[37] K.Y. Li, D.F. Xue, J. Phys. Chem. A 110 (2006) 11332–11337.
[38] T. Krauskopf, S.P. Culver, W.G. Zeier, Chem. Mater. 30 (2018) 1791–1798.
[39] E.P. Ramos, Z.Z. Zhang, A. Assoud, K. Kaup, F. Lalere, L.F. Nazar, Chem. Mater. 30 (2018) 7413–7417.
[40] R.A. Huggins, Ionics 8 (2002) 300–313.
[41] Z. Zhang, J. Zhang, Y. Sun, H. Jia, L. Peng, Y. Zhang, J. Xie, J. Energy Chem. 41 (2020) 171–176.
[42] V. Thangadurai, W. Weppner, Adv. Funct. Mater. 15 (2005) 107–112.
[43] S.P. Ong, Y.F. Mo, W.D. Richards, L. Miara, H.S. Lee, G. Ceder, Energy Environ. Sci. 6 (2013) 148–156.
[44] Y. Wang, W.D. Richards, S.P. Ong, L.J. Miara, J.C. Kim, Y. Mo, G. Ceder, Nat. Mater. 14 (2015) 1026–1032.
[45] M.A. Kraft, S. Ohno, T. Zinkevich, R. Koerver, S.P. Culver, T. Fuchs, A. Senyshyn, S. Indris, B.J. Morgan, W.G. Zeier, J. Am. Chem. Soc. 47 (2018) 16330–16339.
[46] S.P. Culver, R. Koerver, T. Krauskopf, W.G. Zeier, Chem. Mater. 30 (2018) 4179–4192.
[47] Z. Yu, S.-L. Shang, J.-H. Seo, D. Wang, X. Luo, Q. Huang, S. Chen, J. Lu, X. Li, Z.-K. Liu, D. Wang, Adv. Mater. 29 (2017) 1605561.
[48] M. Kraft, S.P. Culver, M. Calderon, F. Boecher, T. Krauskopf, A. Senyshyn, C. Dietrich, A. Zevalkink, J. Janek, W.G. Zeier, J. Am. Chem. Soc. 139 (2017) 10909–10918.
[49] M. Avdeev, M. Sale, S. Adams, R.P. Rao, Solid State Ion. 225 (2012) 43–46.
[50] S. Adams, R.P. Rao, Phys. Status Solidi A 208 (2011) 1746–1753.
[51] S. Adams, R.P. Rao, Bond Valences, Springer Berlin Heidelburg, 2014.
[52] M. Uitz, V. Epp, P. Bottke, M. Wilkening, J. Electroceram. 38 (2017) 142–156.
[53] C.K. Moon, H.-J. Lee, K.H. Park, H. Kwak, J.W. Heo, K. Choi, H. Yang, M.-S. Kim, S.-T. Hong, J.H. Lee, Y.S. Jung, ACS Energy Lett. 3 (2018) 2504–2512.
[54] X. He, Y. Zhu, Y. Mo, Nat. Commun. 8 (2017) 15893.
[55] Z. Zhang, Y. Shao, B. Lotsch, Y.-S. Hu, H. Li, J. Janek, L.F. Nazar, C. Nan, J. Maier, M. Armand, L. Chen, Energy Environ. Sci. 11 (2018) 1945–1976.
[56] K. Oh, D. Chang, B. Lee, D.-H. Kim, G. Yoon, I. Park, B. Kim, K. Kang, Chem. Mater. 30 (2018) 4995–5004.
[57] S. Adams, Solid State Ion. 177 (2006) 1625–1630.